Nano-Micro Letters

e-ISSN 2150-5551
CN 31-2103/TB

ARTICLE

https://doi.org/10.1007/s40820-025-01752-x

Cite as
Nano-Micro Lett.
(2025) 17:235

Received: 13 February 2025
Accepted: 25 March 2025

Thermally Conductive $Ti_3C_2T_x$ Fibers with Superior Electrical Conductivity

Yuxiao Zhou[1], Yali Zhang[1] ✉, Yuheng Pang[1], Hua Guo[1], Yongqiang Guo[1], Mukun Li[1], Xuetao Shi[1], Junwei Gu[1] ✉

HIGHLIGHTS

- The strong covalent crosslinking between trace amounts of borates and the hydroxyl groups of $Ti_3C_2T_x$ significantly reduces interlayer spacing, enhances orientation and compactness, leading to notable improvements in both the mechanical (tensile strength of 188.72 MPa) and electrical properties (7781 S cm^{-1}) of $Ti_3C_2T_x$ fibers.
- Trace amounts of borates can promote the regularization of interfacial structures, reduce interfacial thermal resistance, and significantly enhance the thermal conductivity (13 W m^{-1} K^{-1}) of $Ti_3C_2T_x$ fibers, thus increasing their potential for efficient heat transfer applications.

ABSTRACT High-performance $Ti_3C_2T_x$ fibers have garnered significant potential for smart fibers enabled fabrics. Nonetheless, a major challenge hindering their widespread use is the lack of strong interlayer interactions between $Ti_3C_2T_x$ nanosheets within fibers, which restricts their properties. Herein, a versatile strategy is proposed to construct wet-spun $Ti_3C_2T_x$ fibers, in which trace amounts of borate form strong interlayer crosslinking between $Ti_3C_2T_x$ nanosheets to significantly enhance interactions as supported by density functional theory calculations, thereby reducing interlayer spacing, diminishing microscopic voids and promoting orientation of the nanosheets. The resultant $Ti_3C_2T_x$ fibers exhibit exceptional electrical conductivity of 7781 S cm^{-1} and mechanical properties, including tensile strength of 188.72 MPa and Young's modulus of 52.42 GPa. Notably, employing equilibrium molecular dynamics simulations, finite element analysis, and cross-wire geometry method, it is revealed that such crosslinking also effectively lowers interfacial thermal resistance and ultimately elevates thermal conductivity of $Ti_3C_2T_x$ fibers to 13 W m^{-1} K^{-1}, marking the first systematic study on thermal conductivity of $Ti_3C_2T_x$ fibers. The simple and efficient interlayer crosslinking enhancement strategy not only enables the construction of thermal conductivity $Ti_3C_2T_x$ fibers with high electrical conductivity for smart textiles, but also offers a scalable approach for assembling other nanomaterials into multifunctional fibers.

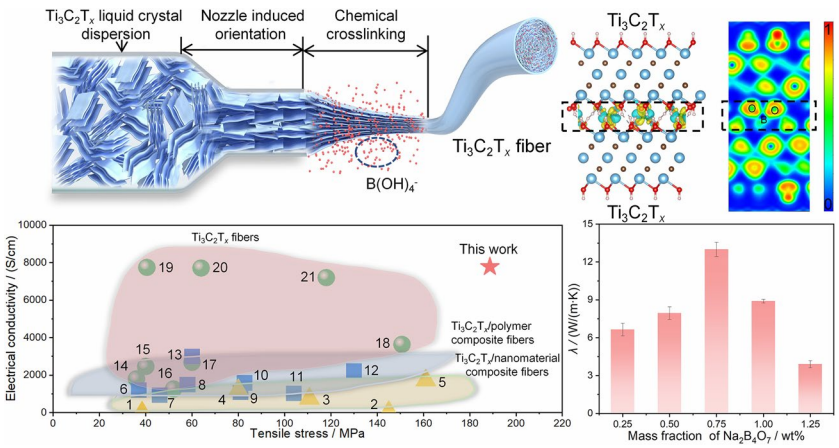

KEYWORDS Thermally conductive $Ti_3C_2T_x$ fibers; Interlayer crosslinking; High electrical conductivity; Density functional theory simulation; Equilibrium molecular dynamics simulation

✉ Yali Zhang, yalizhang@nwpu.edu.cn; Junwei Gu, gjw@nwpu.edu.cn
[1] Shaanxi Key Laboratory of Macromolecular Science and Technology, School of Chemistry and Chemical Engineering, Northwestern Polytechnical University, Xi'an 710072, People's Republic of China

Published online: 27 April 2025

1 Introduction

The rapid development of wearable devices, flexible electronics, and aerospace has highlighted the growing challenges of signal delay and overheating in high-performance electronics, making it difficult for existing fibers to meet the dual needs of fast signal transmission and efficient heat dissipation [1, 2]. Consequently, novel fibers are urgently needed to seamlessly integrate high electrical and thermal conductivity to enhance the signal transmission efficiency and stability of advanced electronics [3–5]. $Ti_3C_2T_x$, as a novel two-dimensional nanomaterial, has emerged as an ideal candidate for producing high-performance fibers due to its exceptional electrical conductivity, thermal conductivity, and mechanical properties [6–8].

Researchers have primarily focused on incorporating $Ti_3C_2T_x$ with polymers or other nanomaterials to fabricate $Ti_3C_2T_x$ composite fibers using scalable wet spinning techniques [9–11]. Gu et al. [12] employed wet spinning to prepare $Ti_3C_2T_x$/polyrotaxane composite fibers, which demonstrated the best overall performance when the mass fraction of $Ti_3C_2T_x$ was 85 wt%, including a tensile strength of 188.7 MPa and an electrical conductivity of 247.5 S cm^{-1}. He et al. [13] fabricated $Ti_3C_2T_x$/reduced graphene oxide composite fibers via wet spinning, having optimal tensile strength (110.7 MPa) and electrical conductivity (743.1 S cm^{-1}) with the $Ti_3C_2T_x$ content of 60 wt%. Although the addition of polymers and other nanomaterials enhances the mechanical properties of $Ti_3C_2T_x$ composite fibers, their inherent non-conductivity or poor conductivity, along with the interface mismatch with $Ti_3C_2T_x$, induces significant electron scattering that severely hampers electron transport [14–16]. As a result, the failure of the composite fibers to achieve the anticipated breakthrough in electrical conductivity occurs despite a high loading of $Ti_3C_2T_x$ [17, 18].

Studies have shown that the issues of introducing non-conductive materials and interface mismatch can be effectively avoided through the fabrication of $Ti_3C_2T_x$ fibers by sole assembling $Ti_3C_2T_x$ nanosheets, which enable a breakthrough in the electrical conductivity of $Ti_3C_2T_x$ fibers [19, 20]. However, the weak interlayer interactions between $Ti_3C_2T_x$ nanosheets pose a significant challenge of poor mechanical properties and easy brittleness for $Ti_3C_2T_x$ fibers during the assembly process [21, 22]. Some efforts have been made to enhance the mechanical properties of $Ti_3C_2T_x$ fibers by reinforcing interlayer connectivity with the hydrogen and ionic bonding [23, 24]. Zhang et al. [24] used an acetic acid aqueous solution as a coagulation bath, in which hydrogen bonding formed by acetic acid and $Ti_3C_2T_x$ nanosheets improved interlayer interactions between the nanosheets, resulting in fibers with good electrical conductivity (4048 S cm^{-1}) and certain mechanical properties (tensile strength < 10 MPa). However, the insufficient interlayer interactions from hydrogen and ionic bonding give rise to multiple defects within $Ti_3C_2T_x$ fibers, including excessive interlayer spacing, microscale porosity, and local disorder of the nanosheets, which constrain the mechanical properties and hinder further enhancement of their electrical conductivity [25, 26]. Furthermore, although $Ti_3C_2T_x$ is theoretically known for its outstanding thermal conductivity, little research can be conducted on the thermal properties of $Ti_3C_2T_x$ fibers [6, 27]. Given the stringent thermal conductivity requirements of high-performance electronics [28, 29], it is crucial for in-depth exploration of the thermal conductivity in $Ti_3C_2T_x$ fibers to address this research gap and facilitate their widespread use in practical electrical and thermal conductivity applications [30, 31].

Compared to hydrogen and ionic bonding, covalent bonds formed through electron sharing offer stronger binding forces and greater structural stability, which are expected to reduce the interlayer spacing, minimize microscopic porosity, and enhance the orientation of the nanosheets, thereby simultaneously improving the mechanical properties, electrical and thermal conductivity for the fibers [32–34]. In nature, the plant cell wall is reinforced by the covalent crosslinking of trace amounts of borate with the hydroxymethyl groups of pectin, which helps enhance the mechanical properties of the wall and strengthen the intercellular network [35, 36]. Building on this inspiration, we propose a strategy of interfacial covalent crosslinking to design and fabricate high-performance $Ti_3C_2T_x$ fibers, where regulating the concentration of $Ti_3C_2T_x$ liquid-crystalline dispersion and the strong covalent crosslinking between borate and the hydroxyl groups on the $Ti_3C_2T_x$ surface enables efficient and continuous assembly of $Ti_3C_2T_x$ fibers. Based on the density functional theory (DFT) calculations, the mechanism by which trace amounts of borate enhance the interlayer interactions, thus improving the interlayer spacing, and promoting the orientation and densification within $Ti_3C_2T_x$

 https://doi.org/10.1007/s40820-025-01752-x

fibers is systematically investigated. The intrinsic factors contributing to the significant enhancement of both electrical conductivity and mechanical properties for $Ti_3C_2T_x$ fibers through the optimization of the nanosheet microstructure are thoroughly discussed. A combination of simulation and experimental validation, including equilibrium molecular dynamics (EMD) simulations, finite element analysis, and crossline testing methods, is employed to deeply analyze the impact of borate content on the thermal conductivity of $Ti_3C_2T_x$ fibers.

2 Experimental Section

2.1 Materials

Ti_3AlC_2 powder (particle size ≈400 mesh) was obtained from 11 Technology Co., Ltd. (Jilin, China). Sodium tetraborate decahydrate ($Na_2B_4O_7{\cdot}10H_2O$), concentrated hydrochloric acid (HCl), lithium fluoride (LiF), and ethyl alcohol were all purchased from Shanghai Macklin Biochemical Technology Co., Ltd. (Shanghai, China).

2.2 Preparation of $Ti_3C_2T_x$ Fibers via Wet Spinning

Firstly, 25 mg mL^{-1} of $Ti_3C_2T_x$ liquid-crystalline dispersion was prepared and placed in the syringe as spinning solution. The $Ti_3C_2T_x$ spinning solution was passed through the nozzle with a diameter of 200 μm under a syringe pump pushing speed of 3.6 mL h^{-1} and extruded into the rotary coagulation bath (rotating speed of 9.42 mm s^{-1}). The coagulants consisted of aqueous/ethanol (7:3 vol/vol) solutions containing different mass fractions of $Na_2B_4O_7$ (0.25, 0.50, 0.75, 1.00, and 1.25 wt%). The $Ti_3C_2T_x$ gel fibers were formed immediately upon contact of the spinning solution with the coagulation bath and were continuously produced as the coagulation bath was rotated. The $Ti_3C_2T_x$ gel fibers were soaked in the coagulation bath for 10 min and then transferred to a washing solution consisting of deionized water and ethanol (7:3 vol/vol). The washed $Ti_3C_2T_x$ gel fibers were collected on a drum and dried in air to obtain $Ti_3C_2T_x$ fibers (B content in $Ti_3C_2T_x$ fibers is given in Table S1), which were stored in a drying chamber.

3 Results and Discussion

3.1 Characterization of $Ti_3C_2T_x$ Dispersion

The schematic illustration of the preparation for $Ti_3C_2T_x$ nanosheets is shown in Fig. 1a. The scanning electron microscope (SEM) image of Ti_3AlC_2 (Fig. 1b) displays its typical layered structure. After selective etching with LiF and HCl, followed by mechanical oscillation and differential centrifugation, the obtained $Ti_3C_2T_x$ nanosheets show an average lateral size of approximately 2.47 ± 0.69 μm, according to SEM image (Fig. 1c) and size distribution (Fig. S2) of $Ti_3C_2T_x$ nanosheets [37]. Moreover, Fig. 1d displays the atomic force microscopy (AFM) image of $Ti_3C_2T_x$ nanosheets with a thickness approximately 1.3 nm and a length-to-width ratio (l/d) greater than 10^3, confirming the successful preparation of single-layer $Ti_3C_2T_x$ nanosheets [38]. The transmission electron microscopy (TEM) image of $Ti_3C_2T_x$ (Fig. 1e) shows that the nanosheets are highly transparent and free of impurities, which indicates the absence of by-products. The single-layer $Ti_3C_2T_x$ nanosheets also maintain a well-ordered crystal structure, as evidenced by clear lattice fringes with a *d*-spacing of 0.26 nm corresponding to the (100) plane observed in the high-resolution TEM (HR-TEM) image (Fig. 1f) [39]. Additionally, the fast Fourier transform (FFT) pattern in the inset of Fig. 1f shows typical hexagonal diffraction spots, which align with the selected area electron diffraction (SAED) pattern (Fig. 1g), further indicating the single-crystal structure of $Ti_3C_2T_x$with hexagonal atomic arrangement [40]. Furthermore, the successful removal of the Al layer in $Ti_3C_2T_x$ after strong acid etching is confirmed by the disappearance of the (104) peak belonging to Ti_3AlC_2 in the X-ray diffraction (XRD) spectrum (Fig. S3a) [41]. As observed from the X-ray photoelectron spectroscopy (XPS) spectrum (Fig. S3b), the Al 2*p* and Al 2*s* peaks associated with Ti_3AlC_2 in $Ti_3C_2T_x$ have distinctly disappeared, and a characteristic peak of the F 1*s* appears at 685 eV, indicating that $Ti_3C_2T_x$ primarily contains four elements: Ti, C, O, and F [42].

According to Onsager's theory, the formation of lyotropic liquid-crystalline phase from two-dimensional nanosheets is governed by the competition between translational and rotational entropy in the dispersion system [43, 44]. The polarized optical microscopy (POM) images of $Ti_3C_2T_x$ dispersion at different concentrations are shown in Fig. 1h-j. At

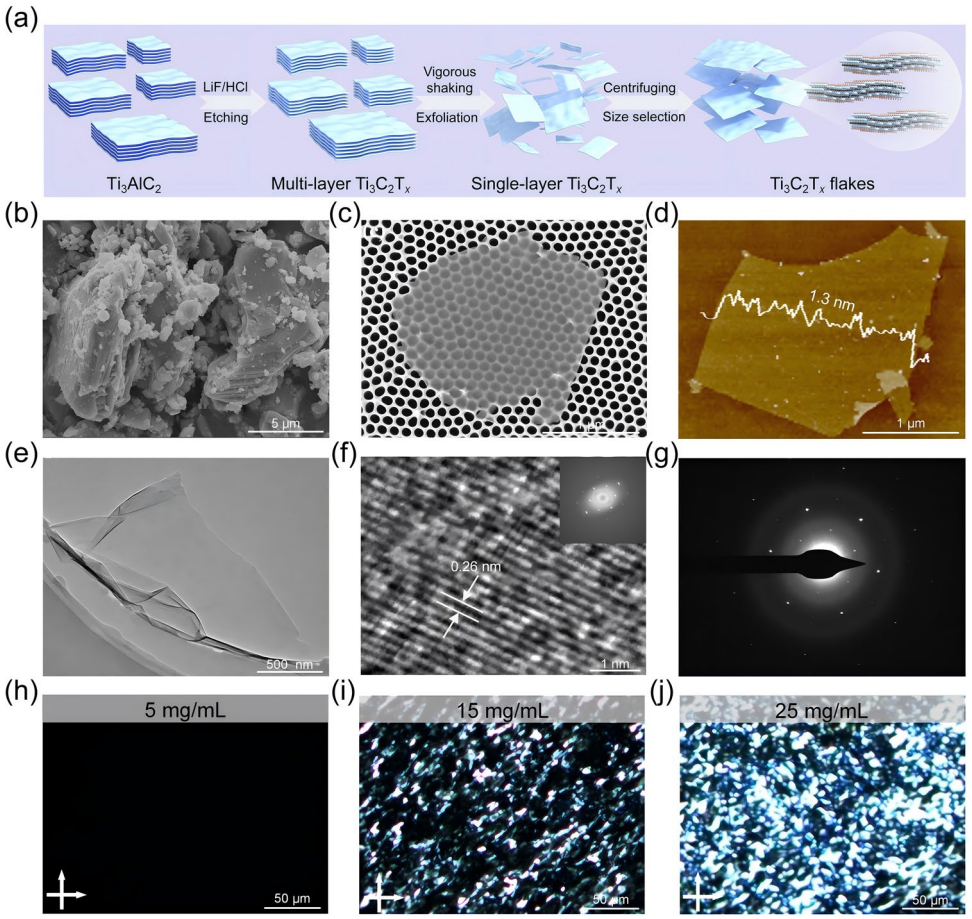

Fig. 1 Preparation and characterization of $Ti_3C_2T_x$ nanosheets and dispersion. **a** Schematic for fabrication of $Ti_3C_2T_x$. **b** SEM image of Ti_3AlC_2. **c** SEM, **d** AFM, **e** TEM, **f** HR-TEM and its FFT diffraction pattern (the inset), and **g** SAED images of $Ti_3C_2T_x$. POM images of $Ti_3C_2T_x$ dispersion at concentrations of **h** 5 mg mL^{-1}, **i** 15 mg mL^{-1}, and **j** 25 mg mL^{-1}

a concentration of 5 mg mL^{-1}, $Ti_3C_2T_x$ dispersion shows no birefringence, and thus remains isotropic (Fig. 1h). This is because, at low concentrations, the large free volume results from the relatively low excluded volume, which refers to the space inaccessible due to the presence of $Ti_3C_2T_x$ nanosheets. In this case, it is difficult for $Ti_3C_2T_x$ nanosheets to rotate and align with translational entropy dominating, instead undergoing random motion and disordered distribution. When the concentration of $Ti_3C_2T_x$ dispersion is 15 mg mL^{-1}, $Ti_3C_2T_x$ dispersion shows appearing birefringent texture under crossed polarizers (Fig. 1i), performing the formation of a nematic liquid-crystalline phase. This is attributed to the increase in excluded volume and corresponding decrease in free volume, which favors rotational entropy. As a result, $Ti_3C_2T_x$ nanosheets begin to align locally and promote the formation of the liquid-crystalline phase. Furthermore, the birefringent texture becomes highly obvious and uniformly distributed at a concentration of 25 mg mL^{-1} (Fig. 1j), signaling that $Ti_3C_2T_x$ dispersion has completely transitioned from isotropic to anisotropic. At this point, the internal nanosheets are locally aligned without aggregation, which provides a unique advantage for the assembly of $Ti_3C_2T_x$ fibers with aligned nanosheets in the wet spinning process. The rheological properties of $Ti_3C_2T_x$ liquid-crystalline dispersion at a concentration of 25 mg mL^{-1} are investigated in Fig. S4. The viscosity of $Ti_3C_2T_x$ liquid-crystalline dispersion decreases with increasing shear rate, displaying shear thinning non-Newtonian behavior, which thus allows the dispersion to flow continuously throughout the nozzle during extrusion (Fig. S4a). Moreover, the significantly higher storage modulus (G′) compared to the loss modulus (G″) across the entire frequency range

 https://doi.org/10.1007/s40820-025-01752-x

(Fig. S4b) indicates the gel-like behavior of $Ti_3C_2T_x$ liquid-crystalline dispersion, enabling it to retain its shape after extrusion and stabilize fiber formation even when shear force is removed [45].

3.2 Fabrication of $Ti_3C_2T_x$ Fibers

Figure 2a illustrates the preparation process of $Ti_3C_2T_x$ fibers. Thanks to the excellent dispersibility and rheological properties of $Ti_3C_2T_x$ liquid-crystalline dispersion [46], the spinning solution was successfully extruded through a fine nozzle into a rotating coagulation bath containing $Na_2B_4O_7$, where interfacial crosslinking facilitated the formation of continuous gel fibers with a stable spinning process, followed by drying to obtain $Ti_3C_2T_x$ fibers, whereas extrusion into a coagulation bath without $Na_2B_4O_7$ did not result in gel fiber formation (Fig. S5 and Movie S1). The fabricated $Ti_3C_2T_x$ fibers are continuously produced with uniform size (Figs. 2b and S6) and exhibit excellent mechanical properties, allowing for manual weaving into textiles (Fig. 2c, d). The overall SEM image of $Ti_3C_2T_x$ fiber (Fig. 2e) shows an average diameter of 23 μm. Cross-sectional and side-view SEM images of the fiber (Fig. 2f, g) demonstrate that $Ti_3C_2T_x$ nanosheets are highly aligned and densely packed along the fiber axis, suggesting the alignment of locally ordered $Ti_3C_2T_x$ nanosheets due to shear forces from the fine nozzle and interfacial crosslinking during the wet spinning process.

From the XPS spectra of $Ti_3C_2T_x$ and $Ti_3C_2T_x$ fiber in Fig. 2h, $Ti_3C_2T_x$ fiber appears a new characteristic peak at 191.8 eV associated with B 1*s* after wet spinning in addition to the F, Ti, O, and C elements compared to $Ti_3C_2T_x$, suggesting that borate may undergo chemical crosslinking with the hydroxyl groups on the $Ti_3C_2T_x$ surface in $Ti_3C_2T_x$ fiber. Figure 2i reveals that the XPS narrow spectra of Ti 2*p* is mainly composed of two parts, Ti $2p_{3/2}$ and Ti $2p_{1/2}$, each of which can be fitted into four components corresponding to Ti–C, Ti^{2+}, Ti^{3+}, and Ti-F. The peaks of Ti^{2+} $2p_{3/2}$ and Ti^{3+} $2p_{3/2}$ shift from 455.6 and 456.6 eV for $Ti_3C_2T_x$ to 455.8 and 457.0 eV for $Ti_3C_2T_x$ fiber, respectively. This is because the electron cloud density around Ti atoms is decreased when B atoms in $Ti_3C_2T_x$ fiber form covalent bonds with Ti atoms via borate ester bonds due to the higher electronegativity of B atoms than Ti atoms, thereby confirming the formation of borate ester covalent bonds between the borate and hydroxyl groups on $Ti_3C_2T_x$ nanosheets [47]. This chemical crosslinking disrupts and replaces the electrostatic repulsion between $Ti_3C_2T_x$ nanosheets, which promotes the transition of $Ti_3C_2T_x$ from liquid-crystalline dispersion to macroscopic fibers. Additionally, the formation of borate ester bonds is directly evidenced by the new characteristic peak of O–B–O at 534.8 eV from $Ti_3C_2T_x$ fiber (Fig. 2j). As indicated by the Fourier transform infrared spectroscopy (FTIR) spectra in Fig. S7, the characteristic peaks of $Ti_3C_2T_x$ at 3426 and 1663 cm^{-1} are attributed to the typical stretching vibrations of –OH and C=O groups, whereas the decreased intensity of the –OH peak at 3426 cm^{-1} and the appearance of the B–O characteristic peak at 1168 cm^{-1} in $Ti_3C_2T_x$ fiber further prove the covalent crosslinking between nanosheets via borate ester bonds. The uniform distribution of Ti element and the sparse distribution of B element in the cross section of $Ti_3C_2T_x$ fiber (Fig. S8) further confirm that borate effectively react with the hydroxyl groups on $Ti_3C_2T_x$ nanosheets during the wet spinning process, and the formation for trace amounts of borate ester covalent bonds facilitates the assembly of $Ti_3C_2T_x$ nanosheets into fibers [48].

3.3 Structural Characterization, Mechanical, and Electrical Properties of $Ti_3C_2T_x$ Fibers

DFT calculations (Fig. 3a) further elucidate the interfacial crosslinking induced by covalent interactions in $Ti_3C_2T_x$ fibers. The optimized structure of the borate ester bond between adjacent $Ti_3C_2T_x$ nanosheets (left) is derived from DFT [49, 50]. The charge density difference (CDD) illustrates the changes in charge density at the interface (middle), where the decreased and increased charge densities are represented in cyan and yellow, respectively [51]. It can be observed that the increase in charge density is primarily localized in the interatomic region between the O atoms on the $Ti_3C_2T_x$ nanosheets and the B atoms introduced by $Na_2B_4O_7$, confirming the formation of B–O covalent bonds. Besides, the B–O bond length between adjacent $Ti_3C_2T_x$ nanosheets is relatively short, ranging from 1.47 to 1.61 Å, which aids the formation of a stable B–O tetrahedral structure between the nanosheets. The electron localization function (ELF) diagram (right) shows the degree of electron localization at the interface, with fully red (1) regions indicating complete localization and fully blue (0) regions

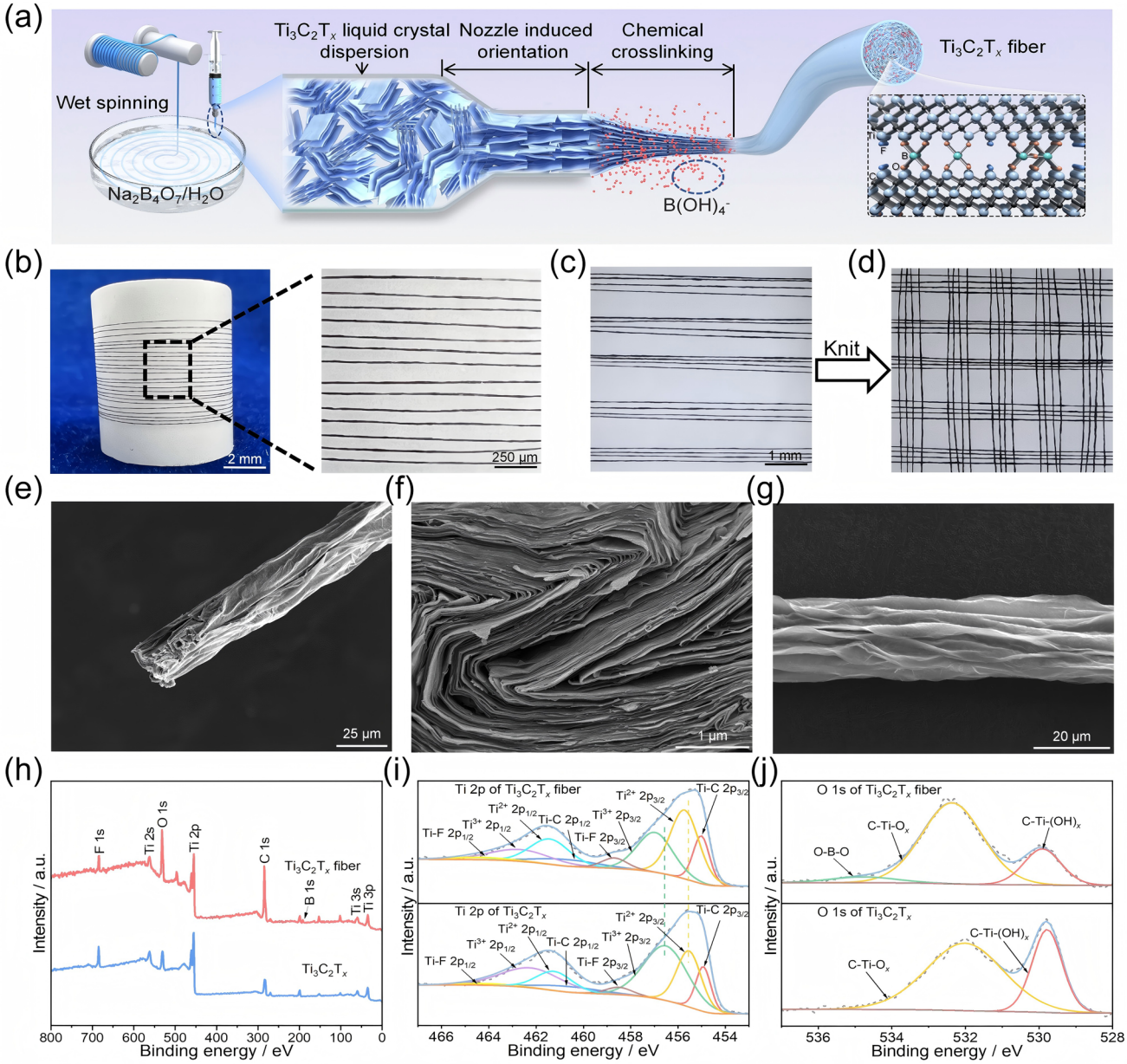

Fig. 2 Fabrication, morphology, and chemical characterization of $Ti_3C_2T_x$ fibers. **a** Schematic for fabricating $Ti_3C_2T_x$ fibers. Photographs of $Ti_3C_2T_x$ fibers **b** wound on the bobbin and **c-d** woven. SEM images of $Ti_3C_2T_x$ fibers: **e** overall, **f** cross section, and **g** side-section views. **h** XPS full spectra, and XPS narrow spectra of **i** Ti 2*p* and **j** O 1*s* of $Ti_3C_2T_x$ powder and $Ti_3C_2T_x$ fiber

indicating no localization [52]. Notably, significant electron localization is shown between the O and B atoms, further corroborating the strong nature of the B–O bond. The XRD patterns of $Ti_3C_2T_x$ fibers (Fig. 3b) show the (002) characteristic peaks at 6.16°, 6.29°, 6.44°, 6.32°, and 6.20° for *c* of 0.25, 0.50, 0.75, 1.00, and 1.25 wt%, respectively. The corresponding average interlayer spacing (d-spacing) was calculated using Bragg's law [53], revealing a trend where the d-spacing of the fibers first decreases and then increases as the $Na_2B_4O_7$ content rises. The covalent crosslinking gradually eliminates the electrostatic repulsion between adjacent $Ti_3C_2T_x$ nanosheets with the increase of $Na_2B_4O_7$ content from 0.25 to 0.75 wt%, which leads to a decline of d-spacing from 14.35 to 13.72 Å. However, when the $Na_2B_4O_7$ content increases from 0.75 to 1.25 wt%, the d-spacing expands from 13.72 to 14.25 Å. This expansion

 https://doi.org/10.1007/s40820-025-01752-x

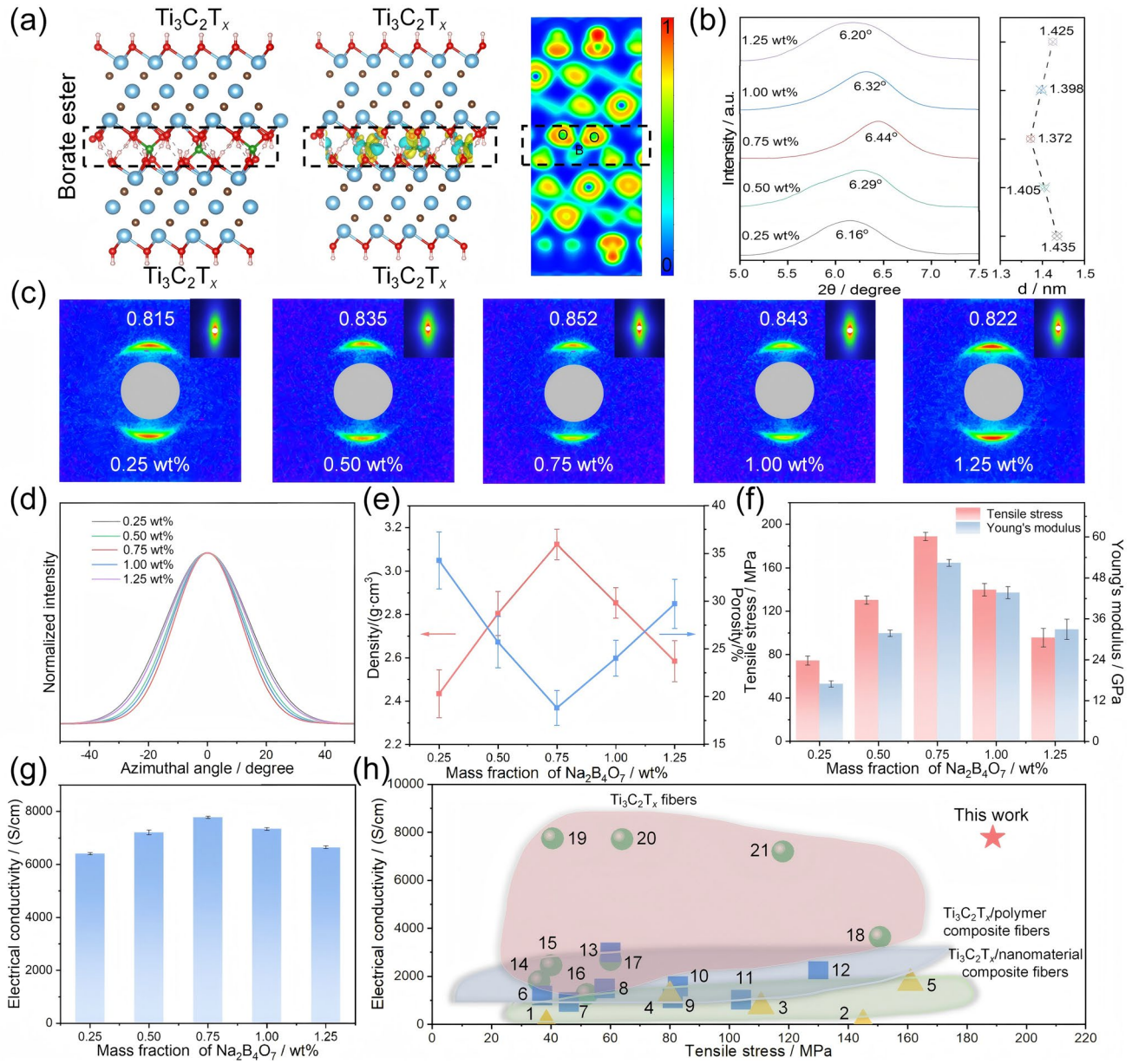

Fig. 3 Structural characterization, mechanical, and electrical properties of $Ti_3C_2T_x$ fibers. **a** DFT calculations of borate ester bond between adjacent $Ti_3C_2T_x$ nanosheets. **b** XRD patterns, **c** WAXS and SAXS (inset) patterns graphs, **d** plots of azimuthal angle according to the WAXS patterns, **e** density and porosity, **f** tensile strength and Young's modulus, and **g** electrical conductivity of $Ti_3C_2T_x$ fibers with different $Na_2B_4O_7$ contents. **h** Comparisons of electrical conductivity versus tensile strength of $Ti_3C_2T_x$ fibers prepared with 0.75 wt% $Na_2B_4O_7$ against reported $Ti_3C_2T_x$-based fibers and $Ti_3C_2T_x$ fibers

is attributed to the excess borate ester bonds that mitigate the electrostatic repulsion, but also act as intercalation impurities, causing the increase in the spacing between $Ti_3C_2T_x$ nanosheets. Moreover, according to the wide-angle X-ray scattering (WAXS), small-angle X-ray scattering (SAXS) patterns (Fig. 3c), and the corresponding plots of azimuthal angle based on WAXS patterns (Fig. 3d) [54], the full width at half maximum (FWHM) of the (002) peak decreases and the orientation orders enhance from 0.815 to 0.852 with the increment of $Na_2B_4O_7$ from 0.25 to 0.75 wt% (Fig. S9). This demonstrates that the stable B–O tetrahedral structure formed between $Ti_3C_2T_x$ nanosheets effectively improves the

alignment and promotes high orientation of the nanosheets. However, as the $Na_2B_4O_7$ content further increases to 1.25 wt%, the FWHM of $Ti_3C_2T_x$ fibers broadens with the orientation order reducing to 0.822, suggesting that excess borate ester covalent bonds hinder the effective alignment of the nanosheets within the fibers. The diameters of $Ti_3C_2T_x$ fibers are decreased and then increased with increasing $Na_2B_4O_7$ (Fig. S10), with the smallest diameter at 0.75 wt% $Na_2B_4O_7$ due to the reduced d-spacing and enhanced orientation order of $Ti_3C_2T_x$ nanosheets. As shown in Fig. 3e, the porosity of $Ti_3C_2T_x$ fibers is significantly reduced to 18.81%, so as to achieve a high density of 3.12 g cm^{-3} with the increment of $Na_2B_4O_7$ to 0.75 wt%, indicating a reduction in interlayer porosity and a denser arrangement of the fibers (Fig. S11). $Na_2B_4O_7$ with more than 0.75 wt% may lead to increased wrinkles and interlayer voids of $Ti_3C_2T_x$ nanosheets, resulting in higher fiber porosity, as evidenced by the increasing intensity of the SAXS pattern (Fig. S12) [40]. Therefore, $Ti_3C_2T_x$ fibers exhibit optimal orientation and density with 0.75 wt% $Na_2B_4O_7$, which significantly contributes to enhancing the overall performance of the fibers.

As shown in Figs. 3f and S13, the tensile strength and Young's modulus of $Ti_3C_2T_x$ fibers exhibit an initial increase followed by a decrease as the $Na_2B_4O_7$ content increases. When the $Na_2B_4O_7$ content is 0.25 wt%, the tensile strength and Young's modulus of $Ti_3C_2T_x$ fibers are 74.40 MPa and 16.91 GPa. It is evident that the dissociation of borate ester covalent bonds dissipates substantial energy during stretching, while the formation of these bonds entitles mechanical properties of $Ti_3C_2T_x$ fibers. As $Na_2B_4O_7$ content increases to 0.75 wt%, $Ti_3C_2T_x$ fibers offer the highest tensile strength and Young's modulus, 1.54 and 2.10 times higher than those of fibers with 0.25 wt% $Na_2B_4O_7$, respectively. This improvement is linked to the augmented borate ester bonds acting as bridging sites, which not only enhance the interactions between adjacent nanosheets, but also simultaneously improve the orientation and density of the nanosheets, thereby promoting optimal load transfer across the nanosheets [55]. However, an excess of borate ester bonds may lead to the aggregation of $Ti_3C_2T_x$ nanosheets when the $Na_2B_4O_7$ content exceeds 0.75 wt%. This aggregation causes stress to concentrate at weak points, including irregular accumulations and voids, which impedes the transfer of stress between nanosheets, thus significantly diminishing tensile strength and Young's modulus of $Ti_3C_2T_x$ fibers. Moreover, the electrical conductivity of $Ti_3C_2T_x$ fibers initially increases and then decreases with increasing $Na_2B_4O_7$ content, reaching a peak of 7781 S cm^{-1} with 0.75 wt% $Na_2B_4O_7$ (Fig. 3g). This is because that the reduced d-spacing and compact stacking of $Ti_3C_2T_x$ nanosheets improve interlayer contact efficiency and support the formation of continuous electron transport pathways. Furthermore, the highly oriented arrangement enables more efficient electron movement between the nanosheets, reducing electron scattering, thereby boosting the electrical conductivity of the fibers. Above all, in comparison to those of previously reported $Ti_3C_2T_x$-based composite fibers and other $Ti_3C_2T_x$ fibers, the resulting macroscopic $Ti_3C_2T_x$ fibers prepared exhibited the highest properties in both tensile strength and conductivity, as summarized in Fig. 3h and Table S2.

3.4 Thermal Conductivity of $Ti_3C_2T_x$ Fibers

The effect of borate ester covalent bonds on the thermal conductivity of $Ti_3C_2T_x$ fibers was explored using both simulation and experimental methods. EMD simulation based on the Green–Kubo method quantified the interfacial thermal resistance (ITR) of $Ti_3C_2T_x$ nanosheets linked by these bonds by building different models with varying $Na_2B_4O_7$ contents (Fig. S14) [56]. Figure 4a illustrates the EMD schematic for the borate ester bonded $Ti_3C_2T_x$ nanosheets, where the system reaches equilibrium when the heat current auto correlation function approaches zero and the temperature remains stable at 300 K. The total energy in these models of different $Na_2B_4O_7$ contents was analyzed to assess the corresponding ITR (Fig. S15). The relationship between the ITR of borate ester bonded $Ti_3C_2T_x$ nanosheets and the concentration of $Na_2B_4O_7$ shows a decrease in ITR as $Na_2B_4O_7$ content increases (Fig. 4b). Specifically, the ITR of $Ti_3C_2T_x$ nanosheets decreases from 7.413×10^{-10} to 4.973×10^{-10} m^2 K W^{-1} when the $Na_2B_4O_7$ content is raised from 0.25 to 1.25 wt%. The reason is that the high crystalline structure and metallic electrical properties of $Ti_3C_2T_x$ nanosheets allow phonons and electrons to serve effectively as thermal carriers for heat transfer. Most importantly, increasing the $Na_2B_4O_7$ content results in a more regular interfacial structure between borate ester bonded $Ti_3C_2T_x$ nanosheets, which enhances the directional movement of phonons and electrons, reducing scattering and lowering ITR. Conversely, the interfacial structure becomes disordered, a phenomenon

 https://doi.org/10.1007/s40820-025-01752-x

that leads to severe phonon and electron scattering, increasing the ITR when $Na_2B_4O_7$ content is reduced [57]. At a $Na_2B_4O_7$ concentration of 0.75 wt%, the ITR is significantly reduced, reaching as low as 6.640×10^{-10} m^2 K W^{-1}. Furthermore, finite element analysis was utilized to simulate the temperature distribution of $Ti_3C_2T_x$ fibers with different $Na_2B_4O_7$ mass fractions under the same heating conditions (bottom temperature of 50 °C for 10 ns) [58], investigating the impact of ITR, d-spacing, orientation orders, and porosity on the heat transfer, as depicted in Figs. 4c, d and S16 [59, 60]. It is clear that the peak temperature of $Ti_3C_2T_x$ fibers first rises and then decreases with an increase of $Na_2B_4O_7$ mass fractions, reaching the highest temperature as well as the fastest heat transfer rate at 0.75 wt% $Na_2B_4O_7$. In contrast, $Ti_3C_2T_x$ fibers exhibit loosely arranged internal layers with more defects and greater air thermal resistance that hinders heat transfer as $Na_2B_4O_7$ mass fraction is 0.25 wt%. The internal layers of $Ti_3C_2T_x$ fibers with 0.75 wt% $Na_2B_4O_7$ are tightly packed and well-oriented coupled with reduced ITR, which enhances physical contact and improves the

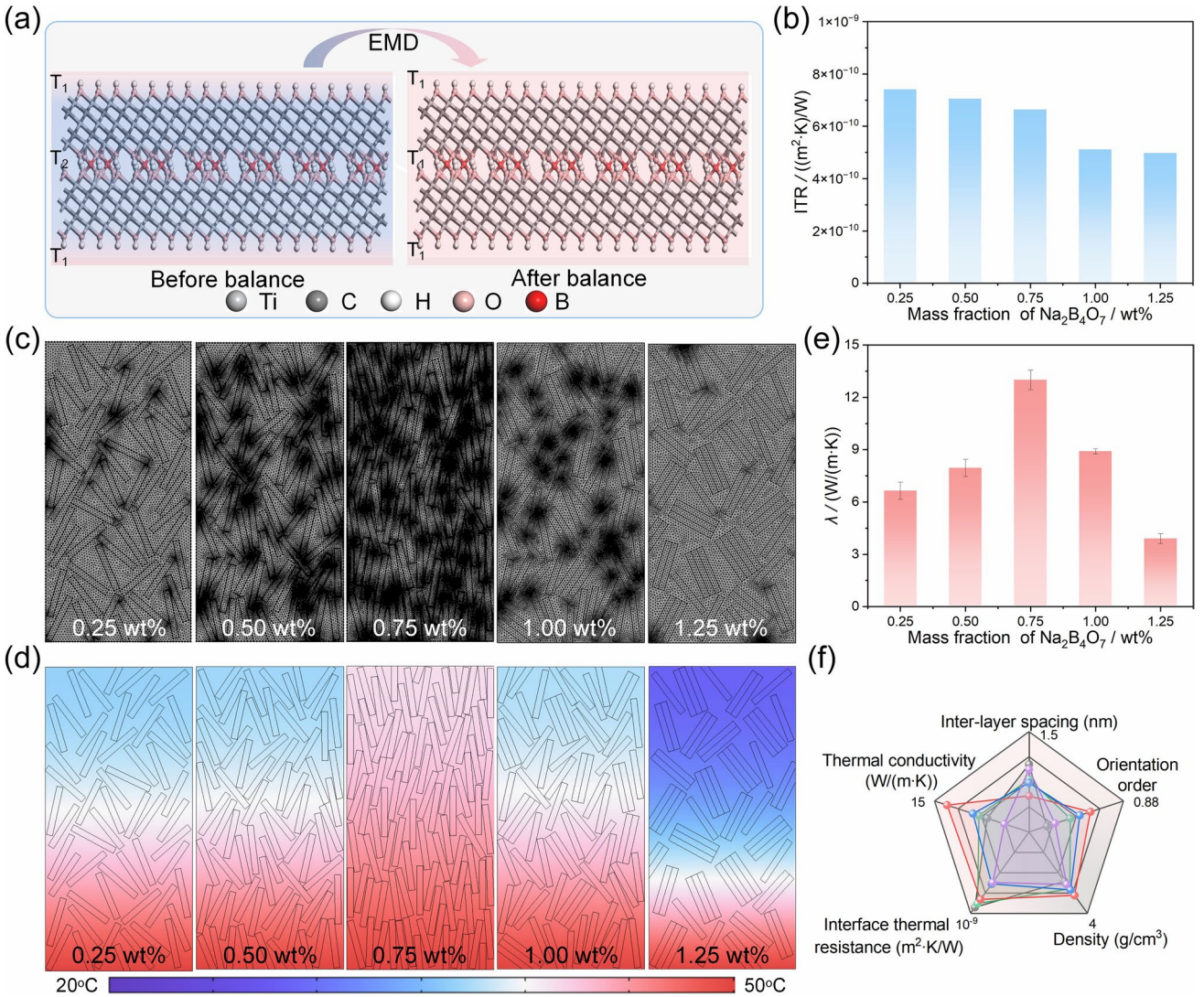

Fig. 4 ITR between $Ti_3C_2T_x$ nanosheets and thermal conductivity of $Ti_3C_2T_x$ fibers. **a** Schematic illustration of EMD simulation of borate ester covalently bonded $Ti_3C_2T_x$ nanosheets. **b** ITR between borate ester covalently bonded $Ti_3C_2T_x$ nanosheets with different $Na_2B_4O_7$ contents obtained by EMD simulation. **c** Extremely fine grid divisions corresponding to the finite element analysis models of $Ti_3C_2T_x$ fibers with different $Na_2B_4O_7$ contents. **d** Temperature distribution of $Ti_3C_2T_x$ fibers with different $Na_2B_4O_7$ contents under the same heating temperature and time simulated by finite element analysis. **e** λ of $Ti_3C_2T_x$ fibers with different $Na_2B_4O_7$ contents. **f** Star-plot of the d-spacing, orientation order, density, ITR, and λ of $Ti_3C_2T_x$ fibers with different $Na_2B_4O_7$ contents

alignment of the nanosheets, thereby significantly improving the heat transfer capabilities of the fibers as a result of the better construction of continuous and effective phonon transport pathways. However, when the $Na_2B_4O_7$ content reaches 1.25 wt%, the low ITR between $Ti_3C_2T_x$ nanosheets cannot compensate for the discontinuity in phonon transport pathways and the increased phonon scattering probability caused by the disorderly aggregation of nanosheets and the higher defect density within the fibers, ultimately leading to a reduction of heat transfer. The thermal conductivity coefficient (λ) of $Ti_3C_2T_x$ fibers was measured using the cross-wire geometry method, where platinum heating wire served both as thermometers and heaters, and $Ti_3C_2T_x$ fiber was mounted as test wire in a cross-geometry with the platinum heating wire [61, 62]. As shown in Fig. 4e, the λ of $Ti_3C_2T_x$ fibers is 6.65 W m^{-1} K^{-1} with 0.25 wt% $Na_2B_4O_7$, and it reaches its maximum value of 13 W m^{-1} K^{-1} when the $Na_2B_4O_7$ content increases to 0.75 wt%. However, further increasing the $Na_2B_4O_7$ concentration to 1.25 wt% results in a decrease of λ to 3.9 W m^{-1} K^{-1}. The variation in λ, consistent with the trends from the finite element analysis, validates the impact of borate ester covalent bonding on the thermal conductivity of $Ti_3C_2T_x$ fibers, where the borate ester bonds not only reduce ITR and improve heat transfer, but also drive the nanosheets into a more ordered and compactly stacked arrangement, thereby forming more efficient phonon transport pathways within the fibers and endowing $Ti_3C_2T_x$ fibers with enhanced thermal conductivity (13 W m^{-1} K^{-1}) (Fig. 4f).

3.5 Joule Heating Performance of $Ti_3C_2T_x$ Fibers

The $Ti_3C_2T_x$ fibers obtained perform high thermal conductivity, mechanical strength, and electrical conductivity as well as superior Joule heating performance. Figure 5a presents the temperature–time curves for single $Ti_3C_2T_x$ fibers with different mass fractions of $Na_2B_4O_7$. It is apparent that all $Ti_3C_2T_x$ fibers immediately generate heat, with surface temperatures rapidly increasing and reaching a steady state around 3 s when applying the working DC voltage of 7 V, indicating a rapid Joule heating response. Notably, $Ti_3C_2T_x$ fibers achieve the highest equilibrium temperature of 85.1°C with 0.75 wt% $Na_2B_4O_7$. The equilibrium temperatures of $Ti_3C_2T_x$ fibers can be finely tuned by applying varying DC voltages from 1 to 9 V, with temperatures rising from 32.1 to 109.3 °C when the content of $Na_2B_4O_7$ is 0.75 wt%, demonstrating their adaptable and tunable Joule heating performance (Fig. 5b). Moreover, the mechanical stability of $Ti_3C_2T_x$ fibers needs to be considered for further practical applications in thermal management [63, 64]. As shown in Fig. 5c, the mechanical stability of $Ti_3C_2T_x$ fibers was confirmed by the results that the temperature–time curves of $Ti_3C_2T_x$ fibers at bending angles from 0° to 180° under a 5 V applied voltage remain consistent across different bending angles with an evenly distributed temperature according to the infrared thermal images. Figure 5d displays infrared thermal images of $Ti_3C_2T_x$ fibers shaped into the letters (npu) under applied voltage, where each letter was formed from fibers of the same length. It is observed that the equilibrium temperatures of the differently shaped letters increase with the applied voltage, exhibiting uniform and consistent temperature distribution. This also proves the excellent flexibility and reliable Joule heating performance of the $Ti_3C_2T_x$ fibers. Additionally, single $Ti_3C_2T_x$ fibers exhibit outstanding cyclic durability, maintaining the performance retention of ~ 94% after 5000 bending cycles (Fig. 5e). These results demonstrate the exceptional and stable Joule heating performance of $Ti_3C_2T_x$ fibers, highlighting their significant potential in wearable thermal management applications.

4 Conclusions

This work presented a simple and efficient interface covalent crosslinking enhancement strategy, where strong covalent interactions between borate and the hydroxyl groups on the $Ti_3C_2T_x$ surface enabled the successful assembly of $Ti_3C_2T_x$ nanosheets into continuous $Ti_3C_2T_x$ fibers via wet spinning. DFT calculations and experimental studies showed that the formation of trace and optimal amounts of borate ester covalent bonding significantly enhanced the interlayer interactions within $Ti_3C_2T_x$ fibers, while dramatically reducing interlayer porosity and promoting sheet alignment, resulting in $Ti_3C_2T_x$ fibers with outstanding mechanical and electrical properties. When the $Na_2B_4O_7$ content is 0.75 wt%, $Ti_3C_2T_x$ fibers exhibit optimal tensile strength of 188.72 MPa and Young's modulus of 52.42 GPa as well as electrical conductivity of 7781 S cm^{-1}. More importantly, EMD simulations and finite element analysis demonstrated that the formation of borate ester covalent bonds reduced the ITR between $Ti_3C_2T_x$

 https://doi.org/10.1007/s40820-025-01752-x

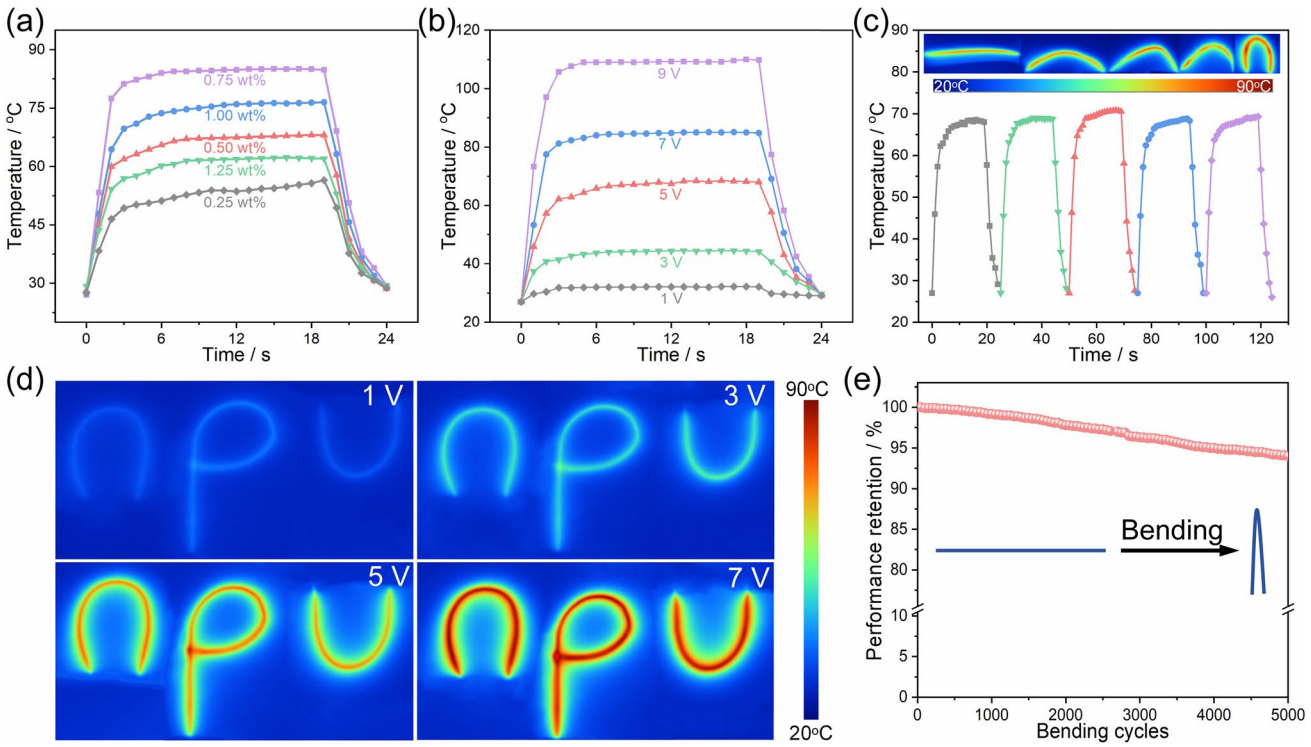

Fig. 5 Joule heating performance of $Ti_3C_2T_x$ fibers. **a** Temperature–time curves of single $Ti_3C_2T_x$ fibers with different $Na_2B_4O_7$ contents when applied DC voltage of 7 V. **b** Temperature–time curves of single $Ti_3C_2T_x$ fibers with 0.75 wt% $Na_2B_4O_7$ when applied DC voltage of 1 ~ 9 V. **c** Temperature–time curves and infrared thermal images of single $Ti_3C_2T_x$ fibers at bending angles of 0° ~ 180°. **d** Infrared thermal images of $Ti_3C_2T_x$ fibers with different letter shapes. **e** Temperature performance retention of $Ti_3C_2T_x$ fibers after 5000 bending cycles

nanosheets, while the low ITR, combined with high alignment and densification of nanosheets, significantly boosted the thermal conductivity of $Ti_3C_2T_x$ fibers, as confirmed by cross-wire geometry method, which achieved optimal λ of 13 W m^{-1} K^{-1} with 0.75 wt% $Na_2B_4O_7$. Additionally, the excellent Joule heating performance of these fibers was displayed. The results reveal that the demonstrated strategy opens up new avenues for the application of $Ti_3C_2T_x$ in the development of fibers with high electrical conductivity and thermal conductivity for smart textiles. Indeed, a great number of multifunctional fibers can be generally assembled through such an effective strategy from various nanomaterials to meet diverse requirements.

Acknowledgements The authors are grateful for the support from the National Natural Science Foundation of China (52403112, 52473083), Natural Science Basic Research Program of Shaanxi (2024JC-TBZC-04), the Innovation Capability Support Program of Shaanxi (2024RS-CXTD-57), Fundamental Research Funds for the Central Universities (D5000240062, D5000240077), Undergraduate Innovation & Business Program in Northwestern Polytechnical University (202410699041), and the Analytical & Testing Center of Northwestern Polytechnical University for performing the SEM, AFM, and TEM tests in this work.

Authors' Contributions Conceptualization was performed by J.W.G., Y.L.Z., and Y.X.Z.; methodology was conducted by Y.X.Z. and Y.H.P.; investigation was done by H.G. and M.K.L.; visualization was presented by Y.X.Z. and Y.Q.G.; writing-original draft was prepared by Y.X.Z., Y.L.Z., and J.W.G.; writing-review & editing were revised by H.G., Y.Q.G, and X.T.S. The manuscript was written through contributions of all authors. All authors have given approval to the final version of the manuscript.

Declarations

Conflict of Interest The authors declare no interest conflict. They have no known competing financial interests or personal relationships that could have appeared to influence the work reported in this paper. Junwei Gu is an editorial board member for Nano-Micro Letters and was not involved in the editorial review or the decision to publish this article. All authors declare that there are no competing interests.

Supplementary Information The online version contains supplementary material available at https://doi.org/10.1007/s40820-025-01752-x.

References

1. C. Hou, M. Zhu, Semiconductors flex thermoelectric power ductile inorganic semiconductors can help enable self-powered wearable electronics. Science **377**, 815–816 (2022). https://doi.org/10.1126/science.add7029
2. A. Sarycheva, A. Polemi, Y. Liu, K. Dandekar, B. Anasori et al., 2D titanium carbide (MXene) for wireless communication. Sci. Adv. **4**(9), eaau0920 (2018). https://doi.org/10.1126/sciadv.aau0920
3. N. Lu, X. Sun, H. Wang, J. Zhang, C. Ma et al., Synergistic effect of woven copper wires with graphene foams for high thermal conductivity of carbon fiber/epoxy composites. Adv. Compos. Hybrid Mater. **7**(1), 29 (2024). https://doi.org/10.1007/s42114-024-00840-7
4. M. Liu, Y. Yang, R. Liu, K. Wang, S. Cheng et al., Carbon nanotubes/graphene-skinned glass fiber fabric with 3D hierarchical electrically and thermally conductive network. Adv. Funct. Mater. **34**(49), 2409379 (2024). https://doi.org/10.1002/adfm.202409379
5. D. Lee, S.G. Kim, S. Hong, C. Madrona, Y. Oh et al., Ultrahigh strength, modulus, and conductivity of graphitic fibers by macromolecular coalescence. Sci. Adv. **8**(16), eabn0939 (2022). https://doi.org/10.1126/sciadv.abn0939
6. Y. Liu, W. Zou, N. Zhao, J. Xu, Electrically insulating PBO/MXene film with superior thermal conductivity, mechanical properties, thermal stability, and flame retardancy. Nat. Commun. **14**(1), 5342 (2023). https://doi.org/10.1038/s41467-023-40707-x
7. Y. Zhang, K. Ruan, K. Zhou, J. Gu, Controlled distributed $Ti_3C_2T_x$ hollow microspheres on thermally conductive polyimide composite films for excellent electromagnetic interference shielding. Adv. Mater. **35**(16), e2211642 (2023). https://doi.org/10.1002/adma.202211642
8. H. Fang, A. Thakur, A. Zahmatkeshsaredorahi, Z. Fang, V. Rad et al., Stabilizing $Ti_3C_2T_x$ MXene flakes in air by removing confined water. Proc. Natl. Acad. Sci. U.S.A. **121**(28), e2400084121 (2024). https://doi.org/10.1073/pnas.2400084121
9. S. Seyedin, S. Uzun, A. Levitt, B. Anasori, G. Dion et al., MXene composite and coaxial fibers with high stretchability and conductivity for wearable strain sensing textiles. Adv. Funct. Mater. **30**(12), 1910504 (2020). https://doi.org/10.1002/adfm.201910504
10. L.X. Liu, W. Chen, H.B. Zhang, L. Ye, Z. Wang, Y. Zhang, P. Min, Z.Z. Yu, Super-tough and environmentally stable aramid. Nanofiber@MXene coaxial fibers with outstanding electromagnetic interference shielding efficiency. Nano-Micro Lett. **14**(1), 111 (2022). https://doi.org/10.1007/s40820-022-00853-1
11. J. Fu, Y. Li, T. Zhou, S. Fang, M. Zhang et al., Large stroke radially oriented MXene composite fiber tensile artificial muscles. Sci. Adv. **11**(2), eadt1560 (2025). https://doi.org/10.1126/sciadv.adt1560
12. J. Gu, F. Li, Y. Zhu, D. Li, X. Liu et al., Extremely robust and multifunctional nanocomposite fibers for strain-unperturbed textile electronics. Adv. Mater. **35**(15), 2209527 (2023). https://doi.org/10.1002/adma.202209527
13. N. He, S. Patil, J. Qu, J. Liao, F. Zhao et al., Effects of electrolyte mediation and MXene size in fiber-shaped supercapacitors. ACS Appl. Energy Mater. **3**(3), 2949–2958 (2020). https://doi.org/10.1021/acsaem.0c00024
14. H. Wang, Y. Wang, J. Chang, J. Yang, H. Dai et al., Nacre-inspired strong MXene/cellulose fiber with superior supercapacitive performance *via* synergizing the interfacial bonding and interlayer spacing. Nano Lett. **23**(12), 5663–5672 (2023). https://doi.org/10.1021/acs.nanolett.3c01307
15. L. Ye, L.-X. Liu, G. Yin, Y. Liu, Z. Deng et al., Highly conductive, hydrophobic, and acid/alkali-resistant MXene@PVDF hollow core-shell fibers for efficient electromagnetic interference shielding and Joule heating. Mater. Today Phys. **35**, 101100 (2023). https://doi.org/10.1016/j.mtphys.2023.101100
16. Q. Yang, Z. Xu, B. Fang, T. Huang, S. Cai et al., MXene/graphene hybrid fibers for high performance flexible supercapacitors. J. Mater. Chem. A **5**(42), 22113–22119 (2017). https://doi.org/10.1039/c7ta07999k
17. G. Zhao, C. Sui, C. Zhao, Y. Zhao, G. Cheng et al., Super-tough MXene/sodium alginate composite fiber felts integrated with outstanding electromagnetic interference shielding and heating properties. Nano Lett. **24**(26), 8098–8106 (2024). https://doi.org/10.1021/acs.nanolett.4c01920
18. G. Yin, J. Wu, L. Ye, L. Liu, Y. Yu, P. Min, Z.Z. Yu, H.B. Zhang, Dynamic adaptive wrinkle-structured silk fibroin/MXene composite fibers for switchable electromagnetic interference shielding. Adv. Funct. Mater. 2314425 (2024).. https://doi.org/10.1002/adfm.202314425
19. Y. Zhou, Y. Zhang, K. Ruan, H. Guo, M. He et al., MXene-based fibers: preparation, applications, and prospects. Sci. Bull. **69**(17), 2776–2792 (2024). https://doi.org/10.1016/j.scib.2024.07.009
20. Z. Xu, C. Gao, Graphene in macroscopic order: liquid crystals and wet-spun fibers. Acc. Chem. Res. **47**(4), 1267–1276 (2014). https://doi.org/10.1021/ar4002813

21. Y. Li, X. Zhang, Electrically conductive, optically responsive, and highly orientated $Ti_3C_2T_x$ MXene aerogel fibers. Adv. Funct. Mater. **32**(4), 2107767 (2022). https://doi.org/10.1002/adfm.202107767
22. W. Eom, H. Shin, R.B. Ambade, S.H. Lee, K.H. Lee et al., Large-scale wet-spinning of highly electroconductive MXene fibers. Nat. Commun. **11**(1), 2825 (2020). https://doi.org/10.1038/s41467-020-16671-1
23. X. Cao, G. Wu, K. Li, C. Hou, Y. Li et al., High-performance Zn^{2+}-crosslinked MXene fibers for versatile flexible electronics. Adv. Funct. Mater. **34**(46), 2407975 (2024). https://doi.org/10.1002/adfm.202407975
24. J. Zhang, S. Uzun, S. Seyedin, P.A. Lynch, B. Akuzum et al., Additive-free MXene liquid crystals and fibers. ACS Cent. Sci. **6**(2), 254–265 (2020). https://doi.org/10.1021/acscentsci.9b01217
25. Y. Zheng, Y. Wang, J. Zhao, Y. Li, Electrostatic interfacial cross-linking and structurally oriented fiber constructed by surface-modified 2D MXene for high-performance flexible pseudocapacitive storage. ACS Nano **17**(3), 2487–2496 (2023). https://doi.org/10.1021/acsnano.2c10065
26. S. Li, Z. Fan, G. Wu, Y. Shao, Z. Xia et al., Assembly of nanofluidic MXene fibers with enhanced ionic transport and capacitive charge storage by flake orientation. ACS Nano **15**(4), 7821–7832 (2021). https://doi.org/10.1021/acsnano.1c02271
27. S. Lakshmanan, V. Jurečič, V. Bobnar, V. Kokol, Dielectric and thermal conductive properties of differently structured $Ti_3C_2T_x$ MXene-integrated nanofibrillated cellulose films. Cellulose **31**(13), 8149–8168 (2024). https://doi.org/10.1007/s10570-024-06105-2
28. Y. Han, K. Ruan, X. He, Y. Tang, H. Guo et al., Highly thermally conductive aramid nanofiber composite films with synchronous visible/infrared camouflages and information encryption. Angew. Chem. Int. Ed. **63**(17), e202401538 (2024). https://doi.org/10.1002/anie.202401538
29. W. Dai, Y. Wang, M. Li, L. Chen, Q. Yan et al., 2D materials-based thermal interface materials: structure, properties, and applications. Adv. Mater. **36**(37), 2311335 (2024). https://doi.org/10.1002/adma.202311335
30. Y. Liu, Y. Wu, X. Wang, Thermal transports in the MXenes family: opportunities and challenges. Nano Res. **17**(8), 7700–7716 (2024). https://doi.org/10.1007/s12274-024-6763-6
31. L. Yan, X. Luo, R. Yang, F. Dai, D. Zhu et al., Highly thermoelectric ZnO@MXene ($Ti_3C_2T_x$) composite films grown by atomic layer deposition. ACS Appl. Mater. Interfaces **14**(30), 34562–34570 (2022). https://doi.org/10.1021/acsami.2c05003
32. S. Wan, X. Li, Y. Chen, N. Liu, Y. Du et al., High-strength scalable MXene films through bridging-induced densification. Science **374**(6563), 96–99 (2021). https://doi.org/10.1126/science.abg2026
33. S. Wan, Y. Chen, S. Fang, S. Wang, Z. Xu et al., High-strength scalable graphene sheets by freezing stretch-induced alignment. Nat. Mater. **20**(5), 624–631 (2021). https://doi.org/10.1038/s41563-020-00892-2
34. L. Ding, T. Xu, J. Zhang, J. Ji, Z. Song et al., Covalently bridging graphene edges for improving mechanical and electrical properties of fibers. Nat. Commun. **15**, 4880 (2024). https://doi.org/10.1038/s41467-024-49270-5
35. Z. An, O.C. Compton, K.W. Putz, L.C. Brinson et al., Bio-Inspired borate cross-linking in ultra-stiff graphene oxide thin films. Adv. Mater. **23**, 3842–3846 (2011). https://doi.org/10.1002/adma.201101544
36. J. Shen, G. Liu, Y. Ji, Q. Liu, L. Cheng et al., 2D MXene nanofilms with tunable gas transport channels. Adv. Funct. Mater. **28**(31), 1801511 (2018). https://doi.org/10.1002/adfm.201801511
37. Q. Chen, S. Huo, Y. Lu, M. Ding, J. Feng et al., Heterostructured Graphene@Silica@Iron phenylphosphinate for fire-retardant, strong, thermally conductive yet electrically insulated epoxy nanocomposites. Small **20**(31), 2310724 (2024). https://doi.org/10.1002/smll.202310724
38. H. Singh, S. Chen, G. Francius, L. Liu, P.S. Lee et al., Understanding in-plane sliding of functionalized $Ti_3C_2T_x$ MXene by *in situ* microscale analysis of electrochemical actuation. Chem. Mater. **36**(19), 9575–9583 (2024). https://doi.org/10.1021/acs.chemmater.4c01597
39. M. He, X. Zhong, X. Lu, J. Hu, K. Ruan et al., Excellent low-frequency microwave absorption and high thermal conductivity in polydimethylsiloxane composites endowed by *Hydrangea*-like CoNi@BN heterostructure fillers. Adv. Mater. **36**(48), 2410186 (2024). https://doi.org/10.1002/adma.202410186
40. T. Zhou, C. Cao, S. Yuan, Z. Wang, Q. Zhu et al., Interlocking-governed ultra-strong and highly conductive MXene fibers through fluidics-assisted thermal drawing. Adv. Mater. **35**(51), e2305807 (2023). https://doi.org/10.1002/adma.202305807
41. L. Ding, Y. Wei, L. Li, T. Zhang, H. Wang et al., MXene molecular sieving membranes for highly efficient gas separation. Nat. Commun. **9**, 155 (2018). https://doi.org/10.1038/s41467-017-02529-6
42. A. Liu, H. Qiu, X. Lu, H. Guo, J. Hu et al., Asymmetric structural MXene/PBO aerogels for high-performance electromagnetic interference shielding with ultra-low reflection. Adv. Mater. **37**(5), e2414085 (2025). https://doi.org/10.1002/adma.202414085
43. Y. Liu, Z. Xu, W. Gao, Z. Cheng, C. Gao, Graphene and other 2D colloids: liquid crystals and macroscopic fibers. Adv. Mater. **29**(14), 1606794 (2017). https://doi.org/10.1002/adma.201606794
44. Y. Xia, T.S. Mathis, M.-Q. Zhao, B. Anasori, A. Dang et al., Thickness-independent capacitance of vertically aligned liquid-crystalline MXenes. Nature **557**(7705), 409–412 (2018). https://doi.org/10.1038/s41586-018-0109-z
45. B. Akuzum, K. Maleski, B. Anasori, P. Lelyukh, N.J. Alvarez et al., Rheological characteristics of 2D titanium carbide (MXene) dispersions: a guide for processing MXenes. ACS Nano **12**(3), 2685–2694 (2018). https://doi.org/10.1021/acsnano.7b08889
46. Q. Zhang, H. Lai, R. Fan, P. Ji, X. Fu et al., High concentration of $Ti_3C_2T_x$ MXene in organic solvent. ACS Nano **15**, 5249–5262 (2021). https://doi.org/10.1021/acsnano.0c10671

47. S. Wan, X. Li, Y. Chen, N. Liu, S. Wang et al., Ultrastrong MXene films *via* the synergy of intercalating small flakes and interfacial bridging. Nat. Commun. **13**, 7340 (2022). https://doi.org/10.1038/s41467-022-35226-0
48. Q. Chen, L. Liu, A. Zhang, W. Wang, Z. Wang et al., An iron phenylphosphinate@graphene oxide nanohybrid enabled flame-retardant, mechanically reinforced, and thermally conductive epoxy nanocomposites. Chem. Eng. J. **454**, 140424 (2023). https://doi.org/10.1016/j.cej.2022.140424
49. T.D. Kühne, M. Iannuzzi, M. Del Ben, V.V. Rybkin, P. Seewald et al., CP2K: an electronic structure and molecular dynamics software package—quickstep: efficient and accurate electronic structure calculations. J. Chem. Phys. **152**(19), 194103 (2020). https://doi.org/10.1063/5.0007045
50. T. Lu, A comprehensive electron wavefunction analysis toolbox for chemists Multiwfn. J. Chem. Phys. **161**(8), 082503 (2024). https://doi.org/10.1063/5.0216272
51. X. Zuo, L. Wang, M. Zhen, T. You, D. Liu et al., Multifunctional TiN-MXene-Co@CNTs networks as sulfur/lithium host for high-areal-capacity lithium-sulfur batteries. Angew. Chem. Int. Ed. **63**(35), e202408026 (2024). https://doi.org/10.1002/anie.202408026
52. W. Lyu, Y. Liu, D. Chen, F. Wang, Y. Li, Engineering the electron localization of metal sites on nanosheets assembled periodic macropores for CO_2 photoreduction. Nat. Commun. **15**(1), 10589 (2024). https://doi.org/10.1038/s41467-024-54988-3
53. L. Huang, H. Wu, L. Ding, J. Caro, H. Wang, Shearing liquid-crystalline MXene into lamellar membranes with super-aligned nanochannels for ion sieving. Angew. Chem. Int. Ed. **63**(6), e202314638 (2024). https://doi.org/10.1002/anie.202314638
54. H. Shin, W. Jeong, T.H. Han, Maximizing light-to-heat conversion of $Ti_3C_2T_x$ MXene metamaterials with wrinkled surfaces for artificial actuators. Nat. Commun. **15**, 10507 (2024). https://doi.org/10.1038/s41467-024-54802-0
55. Q. Chen, Z. Ma, Z. Wang, L. Liu, M. Zhu et al., Scalable, robust, low-cost, and highly thermally conductive anisotropic nanocomposite films for safe and efficient thermal management. Adv. Funct. Mater. **32**(8), 2110782 (2022). https://doi.org/10.1002/adfm.202110782
56. Z. Shi, S. Liao, Y. Wei, L. Li, Theoretical insights into He/CH_4 separation by MXene nanopore. Chem. Eng. Sci. **287**, 119781 (2024). https://doi.org/10.1016/j.ces.2024.119781
57. Q. Chen, Z. Wang, A copper organic phosphonate functionalizing boron nitride nanosheet for PVA film with excellent flame retardancy and improved thermal conductive property. Compos. Part A Appl. Sci. Manuf. **153**, 106738 (2022). https://doi.org/10.1016/j.compositesa.2021.106738
58. H. Liu, C. Du, L. Liao, H. Zhang, H. Zhou et al., Approaching intrinsic dynamics of MXenes hybrid hydrogel for 3D printed multimodal intelligent devices with ultrahigh superelasticity and temperature sensitivity. Nat. Commun. **13**, 3420 (2022). https://doi.org/10.1038/s41467-022-31051-7
59. X. Liu, W. Ma, Z. Qiu, T. Yang, J. Wang et al., Manipulation of impedance matching toward 3D-printed lightweight and stiff MXene-based aerogels for consecutive multiband tunable electromagnetic wave absorption. ACS Nano **17**(9), 8420–8432 (2023). https://doi.org/10.1021/acsnano.3c00338
60. Y. Cheng, Y. Ma, L. Li, M. Zhu, Y. Yue et al., Bioinspired microspines for a high-performance spray $Ti_3C_2T_x$ MXene-based piezoresistive sensor. ACS Nano **14**(2), 2145–2155 (2020). https://doi.org/10.1021/acsnano.9b08952
61. H. Chen, H. Sun, L. Chen, Y. Chen, J. Chen et al., Simultaneous measurement of thermal conductivity and thermal diffusivity of individual microwires by using a cross-wire geometry. Rev. Sci. Instrum. **93**(2), 024901 (2022). https://doi.org/10.1063/5.0074632
62. Q. Chen, Z. Ma, M. Wang, Z. Wang, J. Feng et al., Recent advances in nacre-inspired anisotropic thermally conductive polymeric nanocomposites. Nano Res. **16**(1), 1362–1386 (2023). https://doi.org/10.1007/s12274-022-4824-2
63. X. Wang, Z. Lei, X. Ma, G. He, T. Xu et al., A lightweight MXene-Coated nonwoven fabric with excellent flame Retardancy, EMI Shielding, and Electrothermal/Photothermal conversion for wearable heater. Chem. Eng. J. **430**, 132605 (2022). https://doi.org/10.1016/j.cej.2021.132605
64. Y. Zhang, G. Zhang, Z. Ma, J. Qin, X. Shen, Heterogeneous MXene-based films with graded electrical conductivity towards highly efficient EMI shielding and electrothermal heating. Nano Res. **17**(8), 7264–7274 (2024). https://doi.org/10.1007/s12274-024-6709-z

 https://doi.org/10.1007/s40820-025-01752-x